The Journal of Chemical Physics

Fast-ion-induced secondary ion emission from submicron droplet surfaces studied using a new coincidence technique with forward-scattered projectiles

Cite as: J. Chem. Phys. **153**, 224201 (2020); https://doi.org/10.1063/5.0032301
Submitted: 07 October 2020 • Accepted: 25 November 2020 • Published Online: 10 December 2020

T. Majima, S. Mizutani, Y. Mizunami, et al.

The Journal of Chemical Physics ARTICLE scitation.org/journal/jcp

Fast-ion-induced secondary ion emission from submicron droplet surfaces studied using a new coincidence technique with forward-scattered projectiles

Cite as: J. Chem. Phys. 153, 224201 (2020); doi: 10.1063/5.0032301
Submitted: 7 October 2020 • Accepted: 25 November 2020 •
Published Online: 10 December 2020

View Online Export Citation CrossMark

T. Majima,[1,a)] S. Mizutani,[1] Y. Mizunami,[1] K. Kitajima,[1] H. Tsuchida,[1,2] and M. Saito[1,2]

AFFILIATIONS

[1]Department of Nuclear Engineering, Kyoto University, Kyoto 615-8540, Japan
[2]Quantum Science and Engineering Center, Kyoto University, Uji 611-0011, Japan

[a)]**Author to whom correspondence should be addressed:** majima@nucleng.kyoto-u.ac.jp

ABSTRACT

A mass spectrometric study of secondary ions emitted from droplet surfaces by MeV-energy heavy ion impact was performed to investigate fast-ion-induced molecular reaction processes on liquid surfaces. Herein, a new coincidence technique was developed between secondary ions and scattered projectile ions at a small forward angle. The advantages of this technique were demonstrated by measurement of the collision between 4-MeV C^{3+} and ethanol droplets. Secondary ion emission probabilities were obtained directly from the coincidence data. Notably, this technique enabled positive fragment ions that had not been identified in previous measurements to be observed by suppressing the strong background originating from gas-phase molecules more than 10^4-fold. H^+, H_3O^+, $C_2H_5^+$, and $C_2H_5O^+$ were found to be produced as major positive fragment ions, in addition to minor fragments H_2^+, $C_2H_3^+$, and CH_2OH^+. Production of these ions suggests that competition between rapid hydrogen ion emission from multiply ionized states and intermolecular proton transfer accompanied by fragmentation through protonated ethanol occurs after fast heavy-ion collisions. Clarification of the positive fragment ions also revealed the characteristic features of negative ions. Negative ions were realized to exhibit higher degrees of fragmentation and reactivity compared with positive ions. Furthermore, the energy loss by forward-scattered ions during droplet penetration was used to evaluate the target thickness at a submicron level. Variations in secondary ion yield, mass distribution, and kinetic energies depending on the penetration length were observed below 1 μm. These results highlight the unknown mechanism of these "submicron effects" observed in secondary ion emission processes as a new phenomenon.

I. INTRODUCTION

Fast heavy ions deposit an enormous amount of energy (~keV/nm) in materials along their trajectory, which can cause complex and violent physicochemical reactions. For example, alpha rays from radioisotopes or cosmic rays in space can have destructive effects on materials and living organisms.[1–3] Swift carbon ion beams are now routinely used for cancer therapy. However, details of these complicated reactions remain unclear. The molecular-level mechanism has been examined for decades to obtain a correct understanding of these phenomena and to further improve their application.[4–6] Recently, development of the Monte Carlo simulation has been accelerated as bottom-up research to evaluate the radiation effect.[7,8] Understanding elementary processes and their quantitative information is necessary for calculations. The reactions caused by fast heavy ions cannot be described by a simple extension or superposition of the reactions of low linear energy transfer (LET) radiation. Therefore, it is essential to obtain experimental information about the molecular reactions induced by fast heavy ions.

Secondary ion emission from surfaces has been extensively studied as probes for molecular reactions occurring in heavy ion tracks.[9–11] Mass spectrometry allows a detailed analysis of product ions. As the time scale of secondary ion emission is considered to be in the order of picosecond to sub-nanosecond,[12,13] knowledge of product and intermediate ions generated on that time scale is expected to be obtained. Furthermore, the kinetic energy and emission direction of secondary ions provide further information about the heavy ion track. However, as mass spectrometry requires a high-vacuum environment, special experimental techniques are needed for its application to volatile liquid surfaces. Kosevich *et al.* performed secondary ion mass spectrometry on a liquid surface while melting a frozen target using fast atom bombardment under low-temperature conditions.[14] Kaneda *et al.* succeeded in the secondary ion mass spectrometry of liquid surfaces including ethanol, water, and NaCl aqueous solution using a fast He ion beam by introducing a liquid microjet target.[15,16] Furthermore, Nomura *et al.* applied this technique to an aqueous solution of biomolecules.[17,18]

Recently, we have developed an experimental system using microdroplets as an alternative approach to performing mass spectrometry on liquid surfaces.[19–22] We have reported mass spectra of positive and negative secondary ions from the surface of ethanol droplets.[19,20] Ethanol is a simple molecule but contains rich essential molecular components, such as a carbon–carbon bond, a hydroxy group, and intermolecular hydrogen bonds. Ethanol generates various types of bond dissociation and intermolecular reactions without mixing multiple molecules. Therefore, we consider ethanol to be a suitable model molecule for investigating radiation–chemical reactions. In a previous study, we reported the generation of various types of fragment ions, secondary reaction product ions, and cluster ions emitted from ethanol droplets.[20] However, positive fragment ions could not be identified owing to the abundance of background ions from gas-phase molecules. Although we demonstrated that coincidence measurement of secondary electrons emitted from droplets in the collisions suppressed the background effectively, this method was insufficient for detailed analysis.[19] Elucidation of the positive fragment ions is also important for clarifying the characteristic features of negative fragment ions by comparison.

Another aim of droplet targets is to observe the reaction process at the nanoscale. Studies on the ion beam irradiation of nanoparticles or nanostructured materials are useful not only for applications, such as controlling the properties of nanomaterials and radiosensitizers,[23] but also for investigating nanoscale local collision interactions of energetic ions.[13,24,25] Enhanced sputtering yields have been reported for the irradiation of nanostructures by keV ions. Yang *et al.* reported that the sputtering yield of surface-supported gold nanoparticles with 9.3-nm diameter irradiated by 20-keV C_{60}^{2+} ions was 3.3-fold that of a flat film.[26] Similarly, Greaves *et al.* reported that the sputtering yield of gold nanorods of about 20 nm in diameter irradiated by 80-keV Xe ions was enhanced by more than one order of magnitude.[27] Many simulation studies on the sputtering process of nanoparticles have been performed using molecular dynamics calculations.[28–31] Furthermore, for irradiation by MeV ions, efficient destruction of nanosized droplets by shockwaves has been proposed,[32] which is another potential factor increasing the secondary ion yield in the MeV-energy range. However, droplets applicable in the current experiments have a broad size distribution, with nanometer to micrometer diameters. Using size-selected submicron droplets as an isolated target of ion beams is difficult.

In this study, we have developed a new coincidence technique between secondary ions and forward-scattering projectiles to solve the problems discussed above. This technique is applied to the collision of 4-MeV C^{3+} ions and ethanol droplets as the first measurement. Secondary ion emission probabilities, including positive fragment ions, are obtained by removing gas-phase background signals. Fragmentation processes of positive and negative ions on the droplet surface are discussed. Furthermore, the penetrated target thickness is derived from the energy loss of forward-scattered ions. Although the diameter of the current droplet targets is widely distributed to several micrometers, the coincidence measurement provides selective information depending on the penetration length. In particular, the "submicron effect," namely, variations in the secondary ion emission process below 1 μm, can be examined using the present technique.

II. EXPERIMENTAL METHOD

Figures 1(a) and 1(b) show the top and side views of the experimental setup, respectively. The droplet introduction system and time-of-flight (TOF) mass spectrometer were essentially the same as in our previous report.[20] Ethanol droplets were generated using an ultrasonic atomization method at 1.6 MHz in an argon atmosphere of 1 atm. The argon gas flowed as a carrier gas from a 200-μm aperture into the vacuum chamber. Droplets were transported to the collision chamber through a differential pumping system separated by an aerodynamic lens, a ϕ 2-mm skimmer, and a ϕ 2-mm aperture. The droplet size in the collision area ranges mainly from a few hundred nanometers to a few micrometers, as discussed in Sec. III A. After passing through the collision area, droplets traveled into a liquid nitrogen trap through a ϕ 4-mm aperture. The degree of vacuum in the collision area was 3×10^{-4} Pa during measurements with droplets. A continuous beam of 4-MeV C^{3+}, extracted from a 2-MV Pelletron accelerator at the Quantum Science and Engineering Center of Kyoto University, was used as the projectile. The beam was collimated to 0.4×0.4 mm^2 using two sets of four-jaw slits. The beam divergence was estimated to be less than 0.3 mrad. Secondary ions emitted by the collision of 4-MeV C^{3+} ions were extracted by an electric field in the vertical direction and detected by using a microchannel plate (MCP) detector. Secondary ions were analyzed by using a TOF spectrometer operated under Wiley–McLaren spatial focusing conditions.[33] By reversing the polarity of the extraction electric field, positive or negative secondary ions were measured separately. The detection efficiency of secondary ions was estimated to be 0.42 from the MCP detection efficiency of 0.6 and transmittance of three mesh electrodes of 0.885. The emission probabilities of larger cluster ions might be underestimated owing to the lower MCP detection efficiencies for heavier ions.

In previous experiments, two different start trigger methods have been used for TOF measurements: The first is the beam chopping method, in which the trigger pulse signal is synchronized with

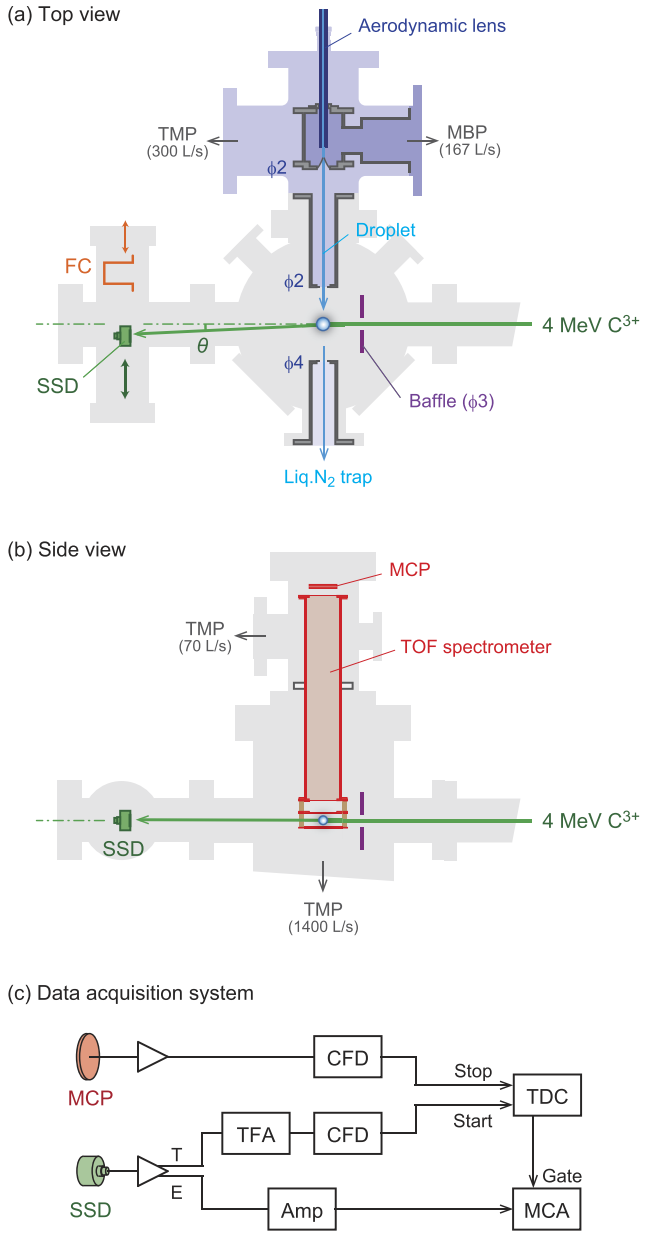

FIG. 1. (a) Top and (b) side views of the experimental setup and (c) measurement circuit diagram.

the chopping deflector to obtain a pulsed ion beam, while the other is the secondary electron coincidence method, which uses the detection signal of secondary electrons emitted from droplets in the collisions. In contrast, the present experiment used the detection signal of projectile ions scattered in the forward direction at scattering angles (θ) of around 6 mrad as the start trigger of measurements. The forward-scattered ions were detected by using a Si semiconductor detector (SSD, Canberra PD50-12-100). A 2-mm-wide slit was placed in front of the SSD with a detection area of 5.6 mm in diameter. Although a smaller scattering angle provides a higher coincidence rate, a halo component of the incident beam starts to mix, causing unwanted random coincidence at scattering angles smaller than 6 mrad.

The measurement circuit diagram is described in Fig. 1(c). The timing signal from the preamplifier connected to the SSD was amplified using a timing-filter amplifier (TFA, ORTEC 474) and then input to a multiple-event time digitizer (TDC, FAST ComTec MCS6A) through a constant-fraction discriminator (CFD, ORTEC 473A) to trigger the measurement. Signals from the MCP detector were input to the TDC through another CFD after a preamplifier. The timings of all MCP signals input during the measurement width of 25.6 μs were recorded for each event in the list mode. The secondary ion probability of each product ion was evaluated by dividing the integrated counts of the corresponding TOF peak by the number of start triggers and correcting with the detection efficiency of 0.42. The energy signal from a preamplifier connected to the SSD was amplified by using a shaping amplifier (Amp, ORTEC 572A). The pulse height was recorded using a multichannel analyzer (MCA, YOKOGAWA WE 7562) in the list mode for each TOF measurement. The transistor–transistor logic (TTL) output from the TDC upon detecting the trigger signal was used as the gate signal for pulse height analysis. After measurements, the TOF and pulse height data were combined to examine their correlation.

III. RESULTS AND DISCUSSION

A. TOF spectra of secondary ions and energy spectra of forward-scattered projectiles

Figures 2(a) and 2(b) show the results of coincidence measurements for positive and negative secondary ions, respectively. Correlations between the TOF of secondary ions and the energy of forward-scattered ions are shown as two-dimensional (2D) histograms. Note that the island shape of each ion in the 2D histogram slightly drifted to the lower-left side. This was due to the trigger timing being slightly delayed as the kinetic energy of the forward-scattered ions decreased. This shift was readily corrected using the flight time of scattered ions in the beamline after collisions at each scattered energy. The projections of the 2D histograms provide the total TOF spectrum of secondary ions and the total energy spectrum of scattered ions.

In the positive TOF spectrum, sequential peaks of protonated cluster ions $[(EtOH)_n + H]^+$ were observed up to $n \sim 15$. The results are consistent with those obtained using the beam chopping method,[20] as shown in Fig. 2(a). This confirms the validity of the present coincidence technique for investigation of the complete picture of secondary ion emission. Large peaks were observed in the small TOF region of the positive TOF spectrum obtained by the beam chopping method. These were attributed to ionized and dissociated ions of evaporated ethanol and the argon carrier gas in the background.[20] The present coincidence measurement suppressed the background by more than four orders of magnitude. Accordingly, the peaks of positive fragment ions originating from droplet surfaces appeared for the first time. The observed ion species are described in detail in Sec. III B.

In the negative TOF spectrum, deprotonated cluster ions $[(EtOH)_n - H]^-$ were observed up to $n \sim 20$. The different series

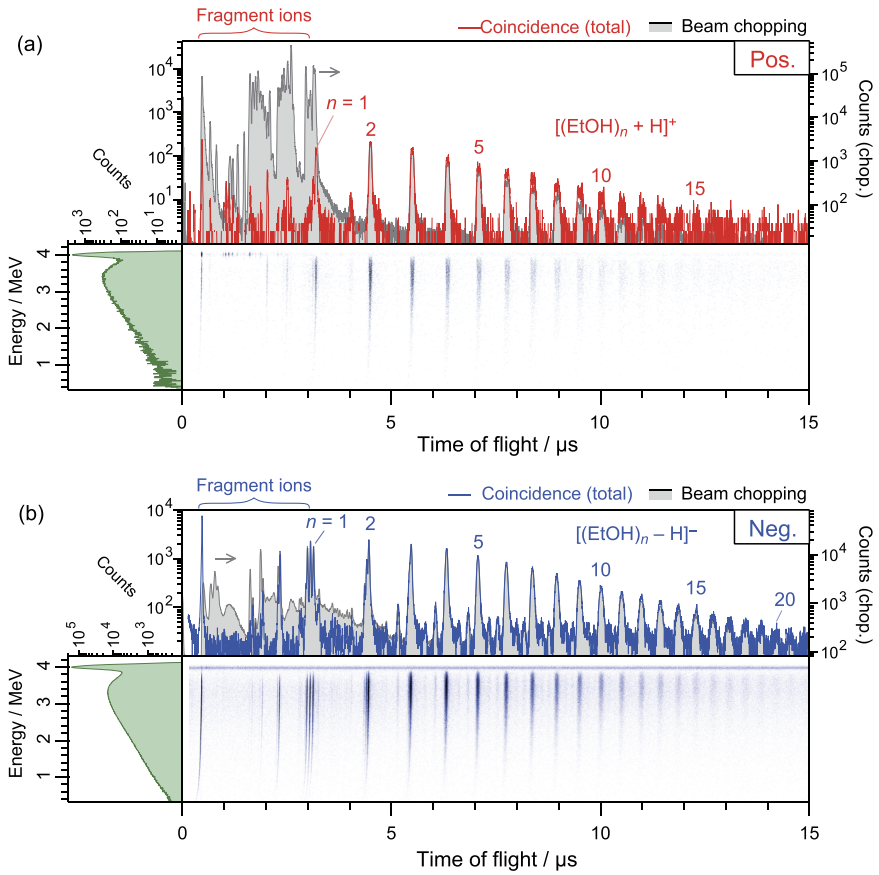

FIG. 2. Two-dimensional correlation map of the energy of forward-scattered ions and TOF for (a) positive and (b) negative secondary ions. Spectra drawn in gray show the results previously obtained with the beam chopping method.[20] The spectra are plotted to be normalized at the n = 2 peak after subtracting the random baseline. The right axes of the TOF spectra represent intensities in the beam chopping method.

of peaks between the $[(EtOH)_n - H]^-$ cluster ions were assigned to $[(H_2O)(EtOH)_n - H]^-$ and $[(CH_2OH)(EtOH)_n - H]^-$.[20] Other ion species, such as fragment ions and secondary reaction product ions, were the same as observed using the beam chopping method.[20] Although the gas-phase background problem was not serious in negative spectra, owing to the low probability of negative ion production in the gas phase, the fragment ion peaks became more clear because false peaks originating from the repeller electrode surface[20] were eliminated.

The energy spectra of forward-scattered ions obtained at scattering angles (θ) of 6 mrad, 20 mrad, and 30 mrad are shown in Fig. 3. The spectrum at 6 mrad is the same as that in Fig. 2(b). The narrow peaks at 4 MeV correspond to ions scattered by two-body collisions with residual gas molecules in the beamline (referred to as "gas-phase peak"). These exhibit almost no energy loss. Broad peaks spreading below 4 MeV correspond to the energy spectra of ions scattered by multiple scattering during droplet penetration (referred to as "droplet peak"). Energy loss ranging from several hundred keV to several MeV was observed. The amount of energy loss determines the penetration length (L) using the range data.[34] Note that L does not directly indicate the diameter of the droplet because L varies depending on the incident point in a droplet. When the penetration length of an event was L, the collided droplet had a diameter of L or larger. The scale of L is described in Fig. 3. The contribution of events with a larger L increased at larger θ values. The energy spectrum at 30 mrad had a maximum at $L \sim 3$ μm. In this study, 6 mrad was adopted to study collision events with $L < 1$ μm. Events with $L > 0.1$ μm can be analyzed separately from the gas phase peak. Herein, regions (i)–(vi) are defined as regions where L is smaller than 0.1 μm, 0.1 μm–0.5 μm, 0.5 μm–1.0 μm, 1.0 μm–2.0 μm, and 2.0 μm–3.0 μm, respectively. Regions (i) and (ii)–(vi) correspond to the gas-phase and droplet peaks, respectively.

B. Mass spectra of fragment ions

Figure 4 shows enlarged views of the TOF spectra in a low-mass range, with the horizontal axis converted into the mass-to-charge ratio (m/z). Figure 4(c) shows the TOF spectrum of positive ions correlated with the gas-phase peak. Peaks of highly ionized argon ions of Ar^{q+} (q = 5–10) and multifragment ions from ethanol molecules, such as H^+, C^+, O^+, and C_2^+, are present. The production of these ions is reasonable because ions scattered by gas-phase molecules have collided with a constituent atom in the molecule with a small impact parameter, leading to multiple ionizations[35,36] and multifragmentation,[36,37] due to the large energy transfer. The negative spectrum correlated with the gas-phase peak is not shown as no peak was observed.

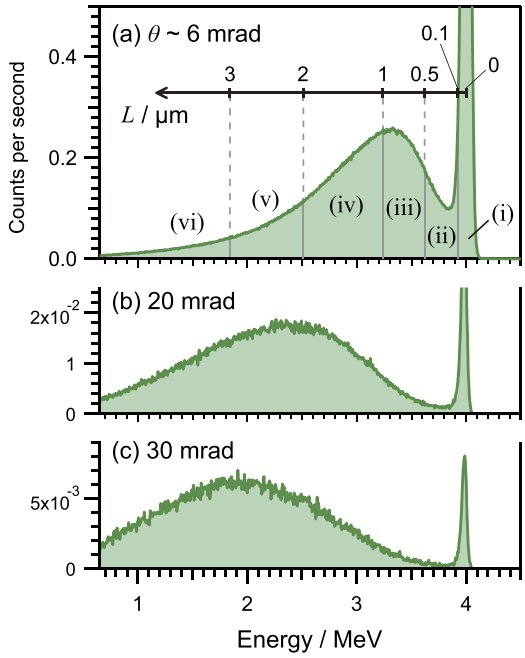

FIG. 3. Energy spectra of forward-scattered ions at scattering angles (θ) of around (a) 6 mrad, (b) 20 mrad, and (c) 30 mrad. Vertical axes indicate the counts per second. The bin width of the spectra is 6.6 keV/chn. *L* indicates the penetration length determined using the range data.[34]

Figures 4(a) and 4(b) show the TOF spectra of positive and negative ions correlated with the droplet peak, respectively. Previously, H_3O^+ production was suggested by the secondary-electron coincidence method.[19] The present method showed the production of other positive fragment ions, namely, H^+, H_2^+, $C_2H_3^+$, $C_2H_5^+$, CH_2OH^+, and $C_2H_5O^+$ (EtO^+), in addition to H_3O^+. Negative fragment ions, such as H^-, CH^-, OH^-, C_2H^-, and $C_2H_mO^-$ (m = 1, 3, and 5), secondary reaction product ions $C_3H_m^-$ (m = 0–2) and $C_4H_m^-$ (m = 0 and 1), and ions with m/z = 58–76 were observed, as reported using the beam chopping method.[20] Table I summarizes the emission probabilities of the secondary ions per single incident ion.

C. Fragmentation processes

Before discussing the fragmentation process of ethanol on the droplet surface, the features of ethanol fragmentation in the gas phase are confirmed. Gas-phase ethanol molecules are known to dissociate into various types of fragment ions, as observed in the spectra of the beam chopping method shown in Fig. 4(a).[20] For example, the most abundant fragment ion from gas-phase ethanol is CH_2OH^+, which is the same as the result of electron impact.[38] This is considered to be produced by C–C bond dissociation as follows:

$$EtOH^+ \rightarrow CH_2OH^+ + CH_3. \quad (1)$$

Furthermore, atomic fragment ions such as H^+ and C^+ are produced with higher relative probabilities in fast heavy-ion collisions

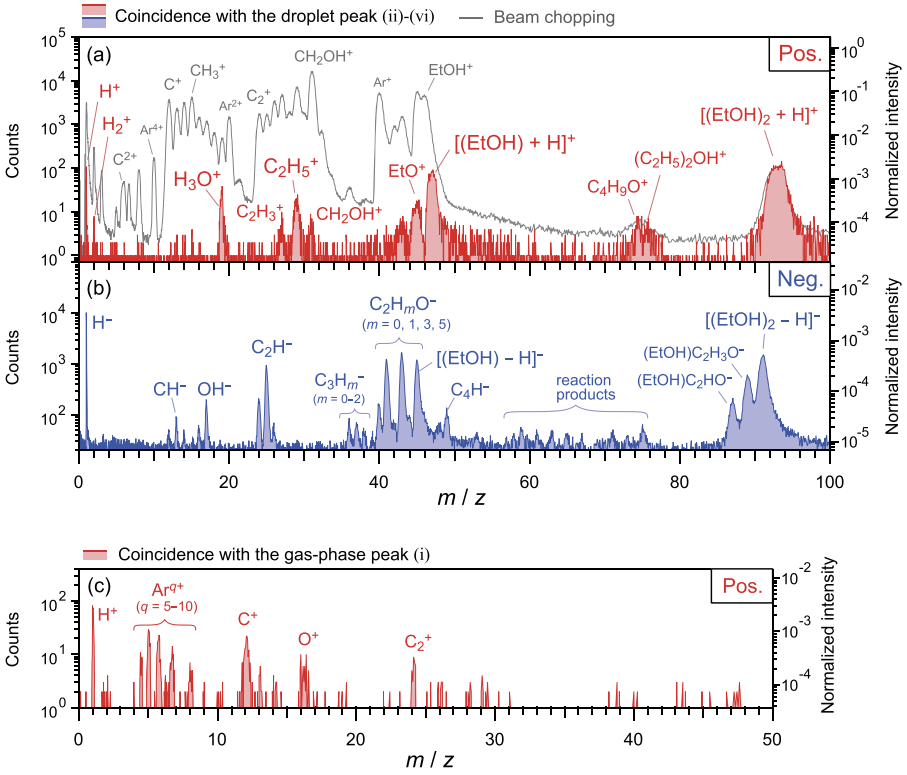

FIG. 4. The low-mass range of TOF mass spectra of (a) positive and (b) negative ions correlated with the droplet peak and (c) positive ions correlated with the gas-phase peak. The right axis represents the counts normalized by the number of start triggers to compare the intensities of (a) and (b). The gray line represents the results previously obtained with the beam chopping method.[20] The intensity is normalized to the present result at $[(EtOH)_2 + H]^+$.

TABLE I. Emission probabilities of secondary ions from ethanol droplet surfaces induced by 4-MeV C^{3+}.

Positive ions	Emission probability	Negative ions	Emission probability
H^+	0.040	H^-	0.0347
H_2^+	0.002	C^-, CH^-, CH_2^-	0.0014
H_3O^+	0.015	O^-, OH^-	0.0019
$C_2H_3^+$	0.004	C_2^-, C_2H^-, $C_2H_2^-$	0.0097
$C_2H_5^+$	0.015	$C_3H_m^-$ (m = 0–3)	0.0017
CH_2OH^+	0.003	C_2O^-, C_2HO^-	0.0119
$C_2H_3O^+$, $C_2H_5O^+$, $[(EtOH) + H]^+$	0.114	$C_2H_3O^-$	0.0146
		$[(EtOH) - H]^-$	0.0121
		C_4^-, C_4H^-,	0.0018
$C_4H_9O^+$, $(C_2H_5)OH^+$	0.010	Reaction products	0.0039
$[(EtOH)_n + H]^+$		$[(EtOH)_n - H]^-$, $(EtOH)_{n-1}C_2H_3O^-$, $(EtOH)_{n-1}C_2HO^-$	
n = 2	0.183	n = 2	0.0326
n = 3	0.151	n = 3	0.0300
n = 4	0.108	n = 4	0.0279
n = 5	0.080	n = 5	0.0212
n = 6	0.067	n = 6	0.0177
n = 7	0.055	n = 7	0.0140
n = 8	0.043	n = 8	0.0113
n = 9	0.038	n = 9	0.0092
n = 10	0.027	n = 10	0.0077
n = 11	0.022	n = 11	0.0061
n = 12	0.015	n = 12	0.0052
		n = 13	0.0045
		n = 14	0.0036
		n = 15	0.0034
Total	1.13	Total	0.355

compared with electron impact. Multifragmentation is enhanced by the Coulomb explosion after multiple ionization in fast heavy-ion collisions.[39]

Compared with gas-phase molecules, the number of ion species generated by the droplet surface is limited and exhibits a completely different distribution. H_3O^+, $C_2H_5^+$, and $C_2H_5O^+$ (or EtO^+) are known to be produced by the dissociation of protonated ethanol molecules $[(EtOH)+H]^+$ (or $EtOH_2^+$).[40–45] Meot-ner and Sieck reported that $EtOH_2^+$ thermally dissociates into H_3O^+ and EtO^+ through C_2H_4 and H_2 loss at temperatures above 600 K.[40] In collision-induced dissociation (CID) experiments of $EtOH_2^+$ at collision energies of 100 eV or less, the production of H_3O^+, $C_2H_3^+$, and $C_2H_5^+$ was reported.[41,42] Mair *et al.* observed that H_3O^+, $C_2H_3^+$, and $C_2H_5^+$ are generated as major fragment ions by surface-induced dissociation (SID) of $EtOH_2^+$ and protonated clusters $[(EtOH)_n + H]^+$ (n = 2, 3) at collision energies of 10 eV–80 eV.[43] Furthermore, H_3O^+ production was observed after ionizing ethanol clusters using fs-laser irradiation[44] and soft x rays,[45] with H_3O^+ considered to be produced via $EtOH_2^+$. The present result, where H_3O^+, $C_2H_3^+$, and $C_2H_5^+$ were observed as dominant fragment ions, provides direct evidence of proton transfer occurring rapidly before dissociation of the ionized ethanol molecules. The dissociation pathways are described as follows:

$$EtOH^+ + EtOH \rightarrow EtOH_2^+ + EtO, \quad (2)$$

$$EtOH_2^+ \rightarrow H_3O^+ + C_2H_4, \quad (3)$$

$$EtOH_2^+ \rightarrow C_2H_5^+ + H_2O, \quad (4)$$

$$EtOH_2^+ \rightarrow C_2H_3^+ + H_2O + H_2. \quad (5)$$

The intensity ratio of H_3O^+, $C_2H_3^+$, and $C_2H_5^+$ in the present study was 44:12:44. This does not match the ratio reported for the SID experiment.[43] Although the ratio from SID varies depending on the collision energy, there are no conditions under which the above three intensity ratios agree with our results. For example, at the collision energy where H_3O^+ and $C_2H_5^+$ were detected to the same extent by SID dissociation, $C_2H_3^+$ was scarcely produced. The SID mechanism was explained by a thermal process in which the internal

energy deposited is statistically distributed to all vibrational degrees of freedom. The discrepancy between the results of SID and the present study indicates that the fragmentation induced by fast heavy ions is different from thermal dissociation owing to the contribution of large electronic excitation.

The production of CH_2OH^+ from $EtOH_2^+$ was not observed in CID[41,42] and SID[43] experiments, probably due to the high reaction barrier.[46] CH_2OH^+ production was reported in CID from protonated dimethyl ether $(CH_3)_2OH^+$, which is an isomer of $EtOH_2^+$.[47] The CH_2OH^+ production in the present study suggests that fast heavy-ion collisions cause isomerization into $(CH_3)_2OH^+$, accompanied by dissociation into CH_2OH^+.

Notably, H^+ was the most abundant fragment ion. Furthermore, H_2^+ was also observed. To our knowledge, the emission of these hydrogen ions from $EtOH_2^+$ has not been reported previously. We suggest that these ions are produced by the Coulomb explosion of multiply ionized ethanol $EtOH^{q+}$ ($q \geq 2$). Multiple ionization is a characteristic process of fast heavy-ion collision. H^+ emission has been confirmed to become the primary process after multiple ionization of gas-phase hydrocarbon molecules.[39] H_2^+ has also been reported to be produced mainly through double ionization.[39] To support this, the kinetic energies (KEs) of H^+ and H_2^+ are examined using the TOF peak structure in Fig. 5, where the horizontal axis is the flight time divided by the square root of m/z. The peak position becomes common and independent of m/z. The deviation from the peak center represents the KE in the direction of the TOF axis. The H^+ peak extends to above 10 eV. This value is consistent with the KE of H^+ emitted from gas-phase C_2H_2[48] and C_2H_6[49] molecules, with the KE distribution peak at around 5 eV with a tail extending to around 20 eV. Although H_2^+ had low counts, the peak width can be evaluated to correspond to about 5 eV–10 eV. This value is also consistent with the KE distribution of H_2^+ emitted from C_2H_6, which peaked at about 4 eV and was distributed up to about 10 eV.[49]

Simultaneously, other small fragment ions observed in the Coulomb explosion of gas-phase molecules, such as CH_n^+ or O^+, were not observed on the droplet surface. This absence proves that competition with rapid intermolecular proton transfer suppresses fragmentation processes that are slower than H^+ and H_2^+ emissions.[50–52] In summary, when an ethanol molecule is (multiply) ionized at the droplet surface, hydrogen ion emission and intermolecular proton transfer competitively proceed on a similar time

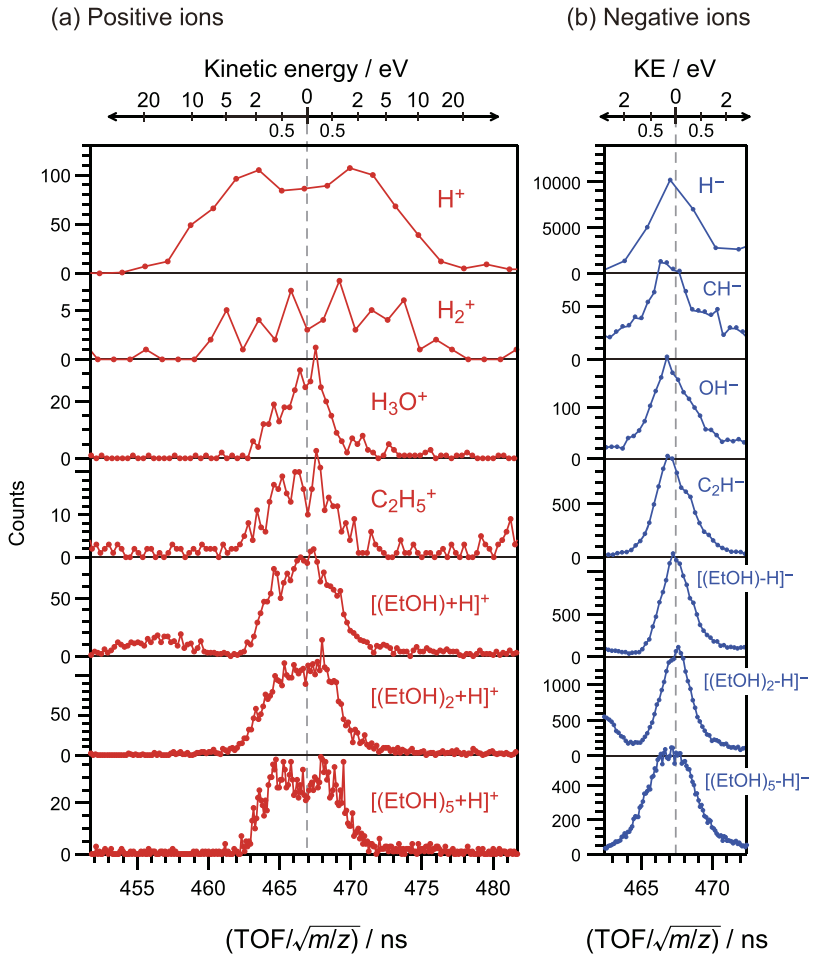

FIG. 5. Expanded views of TOF peaks of (a) positive ions, H^+, H_2^+, H_3O^+, $C_2H_5^+$, and $[(EtOH)_n + H]^+$ (n = 1, 2, and 5), and (b) negative ions, H^-, CH^-, OH^-, C_2H^-, and $[(EtOH)_n - H]^-$ (n = 1, 2, and 5). The horizontal axis is the flight time divided by the square root of m/z. The shift in start time due to the different energy of forward-scattered ions is corrected. The corresponding KE value is shown above the upper axis.

scale. As a result, direct C–O and C–C bond cleavage after multiple ionization are avoided, and further fragmentation proceeds via $EtOH_2^+$.

Elucidating the positive fragment ion species also clarifies the characteristic features of negative fragment ions. First, the negative fragment species were found to be entirely different from the positive species. This difference indicates that the primary production mechanisms of positive and negative fragment ions are not explained by the protonation/deprotonation of common neutral intermediates. Notably, negative ions exhibited a higher degree of dissociation than positive ions. For example, the degree of H_2 desorption from deprotonated ethanol (EtO^-) was greater than that from protonated ethanol ($EtOH_2^+$). Other negative fragment ions, such as CH^-, OH^-, and C_2H^-, also show a large amount of hydrogen desorption. C_2H^- production is attributed to further desorption of a neutral O atom from C_2HO^- in the form of a deprotonated ketene (HCCO), as discussed in our previous report.[20] When comparing the secondary reaction product ions, $C_3H_m^-$ (m = 0–2), $C_4H_m^-$ (m = 0 and 1), and various products with m/z = 58–76 were observed in the negative spectra, while only protonated diethyl ether $(C_2H_5)_2OH^+$ and its dehydrogenated form, $C_4H_9O^+$, were observed as positive ions. Positive ions might be expected to show violent dissociation because they can be generated by ionization near the ion track. However, the dominant fragmentation processes of positive ions were found to be two- or three-body fragmentations. In contrast, negative ions provided smaller fragments and richer secondary reactions. The production of negative fragment ions is considered to be initiated by the attachment of ionized electrons from another molecule. The high reactivity of negative ions is presumably achieved by effective energy transfer to the internal energy of the molecule during the electron attachment process.

D. Submicron effects of secondary ion emission

This section demonstrates how submicron effects, namely, variations in the secondary ion emission processes appearing below 1 μm, are examined using the present technique. As mentioned in Sec. III A, the L value is not always equal to the droplet size because it depends on the incident position in the droplet. However, the distance to the side surface of the droplet (x) is equal to or smaller than $L/2$, as shown in Fig. 6. Therefore, the size effect of the order of L should be studied, although a collision at the center of the droplet of diameter L and a collision at a peripheral region of a larger droplet cannot be distinguished.

Figure 6 shows the total emission probabilities of positive and negative secondary ions from the ethanol droplet per incident ion for regions (ii)–(vi) of scattered energy shown in Fig. 3. These are plotted as a function of the mean penetration length, $\langle L \rangle$, of each region, which was evaluated by considering the energy distribution in each region. Two features were observed. First, the total emission probabilities increased with decreasing L value. For positive ions, the emission probability in region (ii) was 4.2 times larger than that in region (vi). A possible reason for this variation in emission probability is that the present measurements include the forward emission, namely, the secondary ion emission when the projectile is ejected from the back of the droplet. The intensity of the forward emission will decrease with increasing L value because the energy of the projectile ions at exit is small, and the corresponding stopping power declines in this energy range. Another possible factor increasing the emission probability is the geometrical effect, such as different incident angles and lateral emission, which have been suggested to explain high sputtering yields from nanomaterials by keV ion bombardment.[13,30] Similar geometric effects would also be possible at MeV energies. Furthermore, in MeV-energy heavy ion collisions, nanosized droplets have been proposed to collapse effectively due to shockwaves.[32] The present results were qualitatively consistent with the tendencies described above. The second feature observed in Fig. 6 is that positive and negative ions had different dependences on L. The ratio of emission probabilities for negative ions between regions (ii) and (vi) was 2.3, which was smaller than that for positive ions (4.2). This indicates that the submicron effect works differently depending on secondary ion polarity.

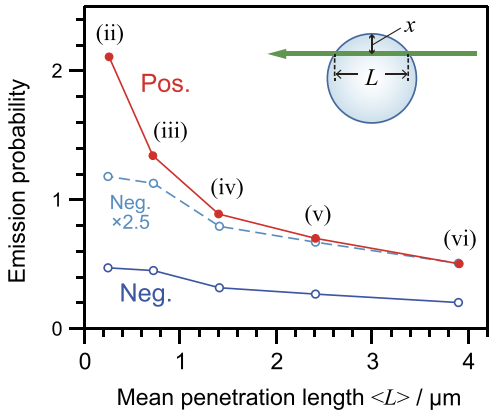

FIG. 6. Total emission probabilities of positive and negative secondary ions from ethanol droplet surfaces per incident ion as a function of the mean penetration length, $\langle L \rangle$, of the forward-scattered ions. To compare the positive and negative distributions, the results of negative ions multiplied by 2.5 are also shown as a dashed line.

To investigate the variation in emission probabilities in detail, the partial probability for each ion species is shown in Fig. 7. The distribution of positive ions did not change depending on the L value. The emission probabilities increased uniformly as L decreased. In contrast, the distribution of negative ions varied depending on the L value. The emission probabilities of cluster ions larger than n = 4 changed almost uniformly depending on the L value, as observed for positive ions, while those of cluster ions with n < 4 exhibited lower rates of increase with decreasing L values. In particular, the emission probabilities for n = 1 (EtO^-) and n = 2 decreased in region (ii). The negative fragment ions and secondary reaction product ions also showed similar behavior to EtO^-. As fragments, secondary reaction products, and cluster ions are supposed to be produced by different mechanisms, it is reasonable to state that these reductions in emission probabilities are not dependent on their production mechanisms but their mass.

For further insight into the secondary ion emission process, the variation in KEs depending on the L value is examined below. TOF peaks of some $[(EtOH)_n + H]^+$ and $[(EtOH)_n - H]^-$ ions were

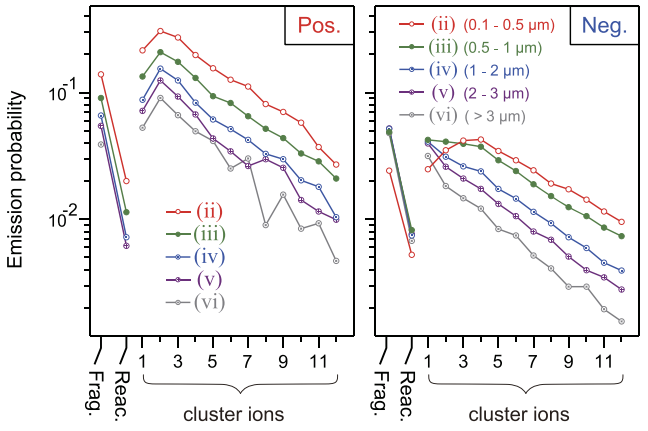

FIG. 7. Emission probability of each secondary ion for regions (ii)–(vi). Frag. and Reac. represent fragment ions and secondary reaction product ions, respectively. Frag. (positive): H^+, H_2^+, H_3O^+, $C_2H_3^+$, $C_2H_5^+$, and CH_2OH^+. Reac. (positive): $(C_2H_5)_2OH^+$. Frag. (negative): H^-, C^-, CH^-, CH_2^-, O^-, OH^-, C_2^-, C_2H^-, and $C_2H_2^-$. Reac. (negative): C_3^-, C_3H^-, $C_3H_2^-$, C_4^-, C_4H^-, and ions with m/z = 58–76. The cluster ions are $[(EtOH)_n + H]^+$ and $[(EtOH)_n - H]^-$, including the hydrogen desorption peak, except for n = 1.

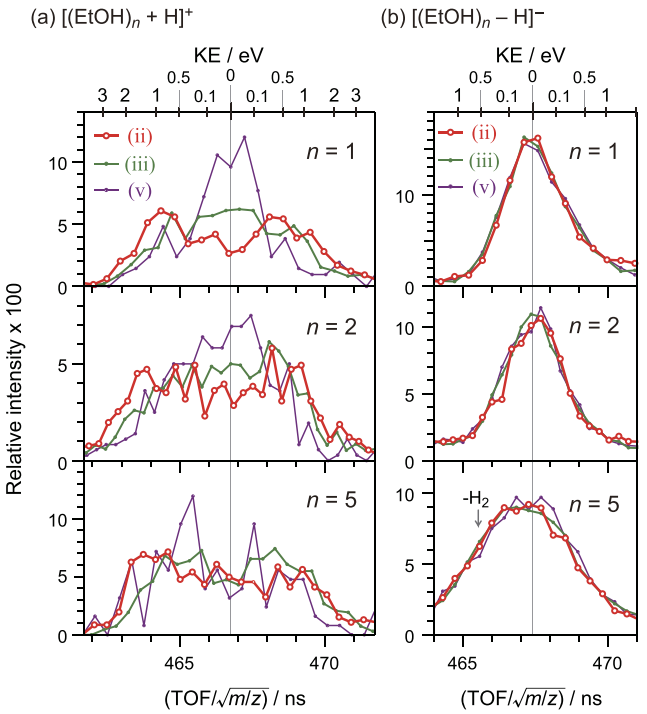

FIG. 8. Expanded views of TOF peaks of (a) protonated ethanol cluster ions $[(EtOH)_n + H]^+$ (n = 1, 2, and 5) and (b) deprotonated ethanol cluster ions $[(EtOH)_n - H]^-$ (n = 1, 2, and 5) separately plotted for different penetration lengths [regions (ii), (iii), and (v)]. The horizontal axis is the flight time divided by the square root of m/z. The shift in start time due to different energies of forward-scattered ions is corrected. The corresponding KE value is shown on the upper axis. To compare peak profiles, the intensity is normalized such that the integrated value of each peak is unity. Note that the $[(EtOH)_5 - H_3]^-$ peak overlaps with the left side of the $[(EtOH)_5 - H]^-$ peak.

plotted separately for different regions of L, as shown in Fig. 8. The horizontal axis was the flight time divided by the square root of m/z, as also used in Fig. 5. The intensity was normalized such that the integrated value of each peak became unity. First, the positive ions show broader peaks than negative ions, as discussed in our previous report.[20] This difference demonstrated the existence of a Coulomb force effect of positive charge generated by ionization along the ion trajectory.

In the present measurement, we observed variations in the peak profile depending on the L value. The peak became broader as L decreased and exhibited even splitting in region (ii). The peaks of H_3O^+ and $C_2H_5^+$ behaved similar to those of $[(EtOH)_n + H]^+$, but are not shown in Fig. 8. This variation in the peak profile indicates an increase in KE at smaller L values or a different distribution of the emission direction of secondary ions depending on the L value, where ions were emitted perpendicular to the TOF axis preferentially when L was large and parallel when L was small. The former scenario would be possible if the positive potential increased with decreasing L. However, this effect seems small because the KEs of negative ions showed little change depending on the L values. In contrast, the latter scenario is expected because a large fraction of collision events with a large L value occur near the droplet center. When secondary ions are emitted in a direction normal to the droplet surface, they are emitted perpendicular to the TOF axis with higher probabilities. When L is small, the emission parallel to the TOF axis increases due to collisions in a peripheral region of the droplets. This feature in the TOF peak structure became obscured for larger cluster ions. This is consistent with previous reports, where large molecular or cluster ions tend to have large radial velocity components from the ion track axis caused by the expansion of heavy ion tracks.[4,53] A large radial velocity obscures the anisotropy of the direction emission depending on the incident position in a droplet.

We expected the peak profiles of light negative ions, including $[(EtOH) - H]^-$ and $[(EtOH)_2 - H]^-$, to show some changes depending on the L value because their emission probabilities decreased at small L values in region (ii). If light negative ions were pulled back by increasing the positive track potential at small L values, decreased KE should be observed. However, no significant changes were observed in the TOF peak structures of $[(EtOH) - H]^-$ and $[(EtOH)_2 - H]^-$. Therefore, we might conclude that the decreased emission probabilities of light negative ions do not originate from the emission dynamics. At this stage, no model can consistently explain all present results regarding L dependences. To further discuss the mechanism, additional investigations, such as measuring the three-dimensional momentum of secondary ions and comparing it with quantitative theoretical calculations, are needed.

IV. SUMMARY

A coincidence measurement method with forward-scattered ions has been developed to obtain detailed experimental insight into the initial molecular reaction and secondary ion emission processes induced by MeV-energy heavy ion collisions on liquid surfaces. As a first measurement, a collision experiment on 4-MeV C^{3+} and ethanol

droplets was performed in this work. This proof-of-principle study demonstrated the advantages of this method as follows. The positive and negative secondary ion emission probabilities for each incident ion were directly obtained by coincidence with forward-scattered ions. In particular, the positive fragment ion species, which were unknown in previous measurements, were revealed by eliminating the strong background of gas-phase peaks. The production of H^+, H_3O^+, $C_2H_5^+$, and EtO^+ ions was identified, in addition to minor ions H_2^+, $C_2H_3^+$, and CH_2OH^+. H^+ and H_2^+ are considered to be released from multiply ionized ethanol ions. This process is probably enhanced by multiple ionization caused by fast heavy-ion collisions. The other positive fragment ions were found to be produced from protonated ethanol $EtOH_2^+$ or its isomers through intermolecular proton transfer. The present results prove the competition between rapid hydrogen ion emission and intermolecular proton transfer accompanied by further fragmentation. Determining the positive fragment ions also clarified the characteristics of the negative fragment ions. The degrees of fragmentation, hydrogen desorption, and secondary reactions of negative ions are greater than those of positive ions, indicating efficient energy transfer to internal energy at the electron attachment.

The measurement of energy loss from the forward-scattered ions provided the penetration length in the droplet for each event. The coincidence measurement was shown to enable the detection of variations in secondary ion yields, distributions, and kinetic energies depending on the droplet penetration length at submicron levels. The overall behavior is difficult to explain with a simple description. The results propose the existence of a new unknown mechanism at the submicron scale. Further improvement of the secondary ion measurements and comparison with theoretical studies is expected to provide a thorough understanding of the submicron effects in secondary ion emission processes. Furthermore, this development is expected to be extended to the measurement of droplets of various solutions, including biomolecules.

ACKNOWLEDGMENTS

This work was supported by JSPS KAKENHI (Grant No. 16K05015). We also acknowledge Mr. Masahiro Naito and Mr. Yoshitaka Sasaki for providing technical support during experiments.

DATA AVAILABILITY

The data that support the findings of this study are available from the corresponding author upon reasonable request.

REFERENCES

[1] *Charged Particle and Photon Interactions with Matter*, edited by A. Mozumder and Y. Hatano (Marcel Dekker, New York, 2003).
[2] *Radiation Damage in Biomolecular Systems*, edited by G. García Gómez-Tejedor and M. C. Fuss (Springer Netherlands, Dordrecht, 2012).
[3] M. Li, G. Gonon, M. Buonanno, N. Autsavapromporn, S. M. de Toledo, D. Pain, and E. I. Azzam, Antioxid. Redox Signaling **20**, 1501 (2014).
[4] B. U. R. Sundqvist, Int. J. Mass Spectrom. Ion Processes **126**, 1 (1993).
[5] *Theory of Heavy Ion Collision Physics in Hadron Therapy*, Advances in Quantum Chemistry Volume 65, edited by D. Belkić (Elsevier/Academic Press, 2013).
[6] *Nanoscale Insights into Ion-Beam Cancer Therapy*, edited by A. V. Solov'yov (Springer, Cham, Switzerland, 2017).
[7] M. A. Bernal, M. C. Bordage, J. M. C. Brown, M. Davídková, E. Delage, Z. El Bitar, S. A. Enger, Z. Francis, S. Guatelli, V. N. Ivanchenko, M. Karamitros, I. Kyriakou, L. Maigne, S. Meylan, K. Murakami, S. Okada, H. Payno, Y. Perrot, I. Petrovic, Q. T. Pham, A. Ristic-Fira, T. Sasaki, V. Štěpán, H. N. Tran, C. Villagrasa, and S. Incerti, Phys. Med. **31**, 861 (2015).
[8] H. Nikjoo, D. Emfietzoglou, T. Liamsuwan, R. Taleei, D. Liljequist, and S. Uehara, Rep. Prog. Phys. **79**, 116601 (2016).
[9] G. Betz and K. Wien, Int. J. Mass Spectrom. Ion Processes **140**, 1 (1994).
[10] D. D. N. B. Daya, P. Demirev, J. Eriksson, A. Hallén, P. Håkansson, R. E. Johnson, J. Kopniczky, R. M. Papaléo, C. T. Reimann, J. Rottler, and B. U. R. Sundqvist, Radiat. Meas. **28**, 101 (1997).
[11] M. Toulemonde, W. Assmann, C. Trautmann, F. Grüner, H. D. Mieskes, H. Kucal, and Z. G. Wang, Nucl. Instrum. Methods Phys. Res., Sect. B **212**, 346 (2003).
[12] J. Sunner, Org. Mass Spectrom. **28**, 805 (1993).
[13] A. V. Krasheninnikov and K. Nordlund, J. Appl. Phys. **107**, 071301 (2010).
[14] M. V. Kosevich, G. Czira, O. A. Boryak, V. S. Shelkovsky, and K. Vékey, J. Mass Spectrom. **33**, 843 (1998).
[15] M. Kaneda, M. Shimizu, T. Hayakawa, Y. Iriki, H. Tsuchida, and A. Itoh, J. Chem. Phys. **132**, 144502 (2010).
[16] M. Kaneda, M. Shimizu, T. Hayakawa, A. Nishimura, Y. Iriki, H. Tsuchida, M. Imai, H. Shibata, and A. Itoh, Nucl. Instrum. Methods Phys. Res., Sect. B **267**, 908 (2009).
[17] S. Nomura, H. Tsuchida, R. Furuya, T. Majima, and A. Itoh, Nucl. Instrum. Methods Phys. Res., Sect. B **389-390**, 28 (2016).
[18] S. Nomura, H. Tsuchida, A. Kajiwara, S. Yoshida, T. Majima, and M. Saito, J. Chem. Phys. **147**, 225103 (2017).
[19] T. Majima, K. Kitajima, T. Nishio, H. Tsuchida, and A. Itoh, J. Phys.: Conf. Ser. **635**, 012021 (2015).
[20] K. Kitajima, T. Majima, T. Nishio, Y. Oonishi, S. Mizutani, J. Kohno, M. Saito, and H. Tsuchida, Nucl. Instrum. Methods Phys. Res., Sect. B **424**, 10 (2018).
[21] K. Kitajima, H. Tsuchida, T. Majima, and M. Saito, Eur. Phys. J. D **72**, 169 (2018).
[22] K. Kitajima, H. Tsuchida, T. Majima, and M. Saito, J. Chem. Phys. **150**, 095102 (2019).
[23] S. Lacombe, E. Porcel, and E. Scifoni, Cancer Nanotechnol. **8**, 9 (2017).
[24] A. P. Mika, P. Rousseau, A. Domaracka, and B. A. Huber, Phys. Rev. B **100**, 075439 (2019).
[25] A. Domaracka, A. Mika, P. Rousseau, and B. A. Huber, in *21st Century Nanoscience: A Handbook*, edited by K. D. Sattler (CRC Press, Boca Raton, Florida, 2020).
[26] L. Yang, M. P. Seah, E. H. Anstis, I. S. Gilmore, and J. L. S. Lee, J. Phys. Chem. C **116**, 9311 (2012).
[27] G. Greaves, J. A. Hinks, P. Busby, N. J. Mellors, A. Ilinov, A. Kuronen, K. Nordlund, and S. E. Donnelly, Phys. Rev. Lett. **111**, 065504 (2013).
[28] R. Kissel and H. M. Urbassek, Nucl. Instrum. Methods Phys. Res., Sect. B **180**, 293 (2001).
[29] T. T. Järvi, J. A. Pakarinen, A. Kuronen, and K. Nordlund, Europhys. Lett. **82**, 26002 (2008).
[30] M. L. Nietiadi, L. Sandoval, H. M. Urbassek, and W. Möller, Phys. Rev. B **90**, 045417 (2014).
[31] L. Sandoval and H. M. Urbassek, Nanoscale Res. Lett. **10**, 314 (2015).
[32] E. Surdutovich, A. Verkhovtsev, and A. V. Solov'yov, Eur. Phys. J. D **71**, 285 (2017).
[33] W. C. Wiley and I. H. McLaren, Rev. Sci. Instrum. **26**, 1150 (1955).
[34] J. F. Ziegler, M. D. Ziegler, and J. P. Biersack, SRIM 2008, available from http://www.srim.org.
[35] M. Saito, Y. Haruyama, K. Yoshida, A. Itoh, and N. Imanishi, J. Phys. B: At., Mol. Opt. Phys. **30**, 115 (1997).
[36] T. Majima, Y. Nakai, T. Mizuno, H. Tsuchida, and A. Itoh, Phys. Rev. A **74**, 033201 (2006).

[37]T. Mizuno, D. Okamoto, T. Majima, Y. Nakai, H. Tsuchida, and A. Itoh, Phys. Rev. A **75**, 063203 (2007).
[38]NIST Mass Spectrometry Data Center, W. E. Wallace, "Mass Spectra," in *NIST Chemistry WebBook, NIST Standard Reference Database Number 69*, edited by P. J. Linstrom and W. G. Mallard (National Institute of Standards and Technology, Gaithersburg, MD, 2020) (retrieved September 10, 2020).
[39]T. Majima, T. Murai, T. Kishimoto, Y. Adachi, S. O. Yoshida, H. Tsuchida, and A. Itoh, Phys. Rev. A **90**, 062711 (2014).
[40]M. Meot-ner (Mautner) and L. Wayne Sieck, Int. J. Mass Spectrom. Ion Processes **92**, 123 (1989).
[41]P. H. Dawson, Int. J. Mass Spectrom. Ion Phys. **50**, 287 (1983).
[42]A. G. Harrison, Org. Mass Spectrom. **22**, 637 (1987).
[43]C. Mair, M. Lezius, Z. Herman, and T. D. Märk, J. Chem. Phys. **118**, 7090 (2003).
[44]K. Hoshina and M. Tsuge, Chem. Phys. Lett. **489**, 154 (2010).
[45]Y. Tamenori, K. Okada, K. Tabayashi, A. Hiraya, T. Gejo, and K. Honma, Chem. Phys. Lett. **433**, 43 (2006).
[46]D. J. Swanton, D. C. J. Marsden, and L. Radom, Org. Mass Spectrom. **26**, 227 (1991).
[47]M. F. Jarrold, N. J. Kirchner, S. Liu, and M. T. Bowers, J. Phys. Chem. **90**, 78 (1986).
[48]S. Yoshida, T. Majima, T. Asai, M. Matsubara, H. Tsuchida, M. Saito, and A. Itoh, Nucl. Instrum. Methods Phys. Res., Sect. B **408**, 203 (2017).
[49]S. Yoshida, T. Majima, H. Tsuchida, and M. Saito, X-Ray Spectrom. **49**, 177 (2020).
[50]S. Shimizu, V. Zhakhovskii, F. Sato, S. Okihara, S. Sakabe, K. Nishihara, Y. Izawa, T. Yatsuhashi, and N. Nakashima, J. Chem. Phys. **117**, 3180 (2002).
[51]S. Bubin, M. Atkinson, K. Varga, X. Xie, S. Roither, D. Kartashov, A. Baltuška, and M. Kitzler, Phys. Rev. A **86**, 043407 (2012).
[52]E. Livshits, I. Luzon, K. Gope, R. Baer, and D. Strasser, Commun. Chem. **3**, 49 (2020).
[53]W. Ens, B. U. R. Sundqvist, P. Håkansson, A. Hedin, and G. Jonsson, Phys. Rev. B **39**, 763 (1989).